


Emission of Photon Multiplets by a dc-Biased Superconducting Circuit

G. C. Ménard^{1,†,§}, A. Peugeot^{1,§}, C. Padurariu², C. Rolland¹, B. Kubala^{2,3}, Y. Mukharsky¹, Z. Iftikhar¹, C. Altimiras¹, P. Roche¹, H. le Sueur¹, P. Joyez¹, D. Vion¹, D. Esteve¹, J. Ankerhold^{2,‡} and F. Portier^{1,*}

¹DSM/IRAMIS/SPEC, CNRS UMR 3680, CEA, Université Paris-Saclay, 91190 Gif sur Yvette, France

²Institute for Complex Quantum Systems and IQST, University of Ulm, 89069 Ulm, Germany

³Institut of Quantum Technologies, German Aerospace Center (DLR), 89069 Ulm, Germany

 (Received 19 November 2021; revised 11 February 2022; accepted 14 March 2022; published 8 April 2022)

We observe the emission of bunches of $k \geq 1$ photons by a circuit made of a microwave resonator in series with a voltage-biased tunable Josephson junction. The bunches are emitted at specific values V_k of the bias voltage, for which each Cooper pair tunneling across the junction creates exactly k photons in the resonator. The latter is a microfabricated spiral coil which resonates and leaks photons at 4.4 GHz in a measurement line. Its characteristic impedance of 1.97 k Ω is high enough to reach a strong junction-resonator coupling and a bright emission of the k -photon bunches. We show that a rotating-wave approximation treatment of the system accounts quantitatively for the observed radiation intensity, from $k = 1$ to 6, and over 3 orders of magnitude when varying the Josephson energy E_J . We also measure the second-order correlation function of the radiated microwave to determine its Fano factor F_k , which in the low E_J limit confirms with $F_k \simeq k$ the emission of k -photon bunches. At larger E_J , a more complex behavior is observed in quantitative agreement with numerical simulations.

DOI: [10.1103/PhysRevX.12.021006](https://doi.org/10.1103/PhysRevX.12.021006)

Subject Areas: Mesoscopics, Quantum Physics, Superconductivity

I. INTRODUCTION

The pioneering work of Max Planck on light emission by hot matter led to the recognition of the granular character of light and to the concept of photon. The quantum theory then explained how electrons in atoms occupy discrete energy eigenstates and how transitions between these states radiate single photons. The corresponding photon emission rate is governed by the light-electrical charge coupling strength, measured by the ratio between the vacuum impedance Z_0 and the quantum of resistance $R_K = h/e^2$, namely, the fine structure constant $\alpha_{\text{QED}} = Z_0/2R_K \simeq 1/137$ [1]. The smallness of α_{QED} places usual light emission in a perturbative regime of quantum electrodynamics (QED).

On the other hand, emission of photon multiplets (bunches with always the same number k of photons) in a single event only occurs in special circumstances, as in

atomic cascades, or in nonlinear media able to split single photons into several photons. For instance, parametric down-conversion is commonly used to produce pairs of strongly correlated photons, and emission of photon triplets has even been achieved [2,3]. Here, we consider multiphoton emission in the generic context of electrical circuits with a quantum coherent conductor steadily maintained out of equilibrium by a dc voltage source, and producing photons each time this conductor is traversed by a charge carrier [4–7]. The resulting QED of this type of circuits with designed light-matter coupling strength [6,8–15] can provide, e.g., sub-Poissonian photon sources [16–22], novel types of lasers [23–26], near-quantum-limited amplifiers [27,28], squeezed radiation [9,10,29], and interesting quantum state engineering resources [30–33].

The particular circuit of this work and the principle of the experiment are shown in the schematics of Fig. 1(a). A tunable Josephson junction (JJ) with Josephson energy E_J , biased at a dc voltage V , is placed in series with a microwave resonator of frequency $\nu_R = \omega_R/2\pi$ and characteristic impedance Z_R . In addition, the resonator is capacitively overcoupled to a measurement line, into which photons leak at an energy decay rate $\kappa = \omega_R/Q$. By design, Z_R is of the order of R_K , thus placing microwave emission in the nonperturbative regime far away from the conventional QED regime. Note that V is kept much smaller than the superconducting gap voltage of the JJ electrodes, so that no electrons can tunnel through the JJ at low temperature. Only Cooper pairs with charge $-2e$ can thus tunnel,

*Deceased.

[†]gerbold.menard@gmail.com

[‡]joachim.ankerhold@uni-ulm.de

[§]These authors contributed equally to this work.

Published by the American Physical Society under the terms of the [Creative Commons Attribution 4.0 International license](https://creativecommons.org/licenses/by/4.0/). Further distribution of this work must maintain attribution to the author(s) and the published article's title, journal citation, and DOI.

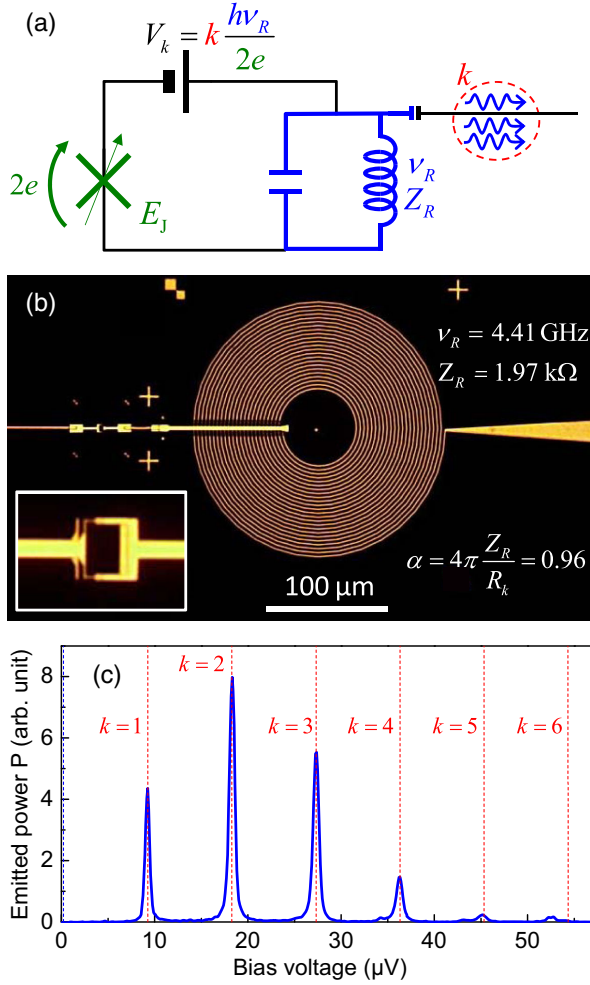


FIG. 1. Principle of the experiment and first observation of multiphoton emission up to $k = 5$ (run 1). (a) A tunable Josephson junction (JJ) with energy E_J (green cross) is connected in series with a dc voltage source V and a microwave resonator (blue) of frequency ν_R and characteristic impedance Z_R . Current can flow only at certain values V_k of V for which the energy $2eV_k$ of a Cooper pair transferred across the circuit is entirely transformed into an integer number k of photons in the resonator. Is the field leaking out of the resonator quantitatively understood and does it display k -photon bunches? (b) Optical micrograph of the sample showing a SQUID (magnetically tunable JJ, main picture and inset) connected to a high inductance coil (resonator). The electrical parameters are indicated and lead to a giant effective fine structure constant $\alpha \sim 1$. The bias and measuring lines are schematized in Fig. 4. (c) Emitted power measured as a function of the bias voltage V for a Josephson energy E_J large enough to observe emission peaks up to $k = 5$. The black and red vertical dotted lines indicate the offset voltage and the V_k values, respectively. Note that the small peak visible below V_6 is a spurious emission attributed to a high-frequency mode of the circuit.

provided that the energy $2eV$ delivered by the source is entirely converted into an integer number k of photons in the resonator. These inelastic processes occur only at particular bias values V_k such that

$$2eV_k = k h \nu_R, \quad k = 1, 2, 3, \dots \quad (1)$$

The aim of this experimental work is to obtain these k -photon bunches with a high brightness, to compare the photon fluxes to theoretical predictions, and to obtain a signature of the k granularity.

II. THEORY

The Hamiltonian of the circuit is the sum of the resonator Hamiltonian $\hbar\omega_R(\hat{a}^\dagger\hat{a} + 1/2)$, with $\hat{a}^{(\dagger)}$ the photon annihilation (creation) operator, and of the Josephson Hamiltonian $\hat{H}_J = -E_J \cos \hat{\phi}_J$ with ϕ_J the superconducting phase difference across the JJ. The voltage source imposes a total phase difference across the circuit increasing linearly with time t , $\phi_V = \omega_J t = \hat{\phi}_J + \hat{\phi}_R$, with $\nu_J = \omega_J/2\pi = 2eV/h$ the Josephson frequency, $\hat{\phi}_R = \sqrt{\alpha}(\hat{a}^\dagger + \hat{a})$ the phase across the resonator, and $\alpha = 4\pi Z_R/R_k$. The time-dependent Hamiltonian of the circuit is thus

$$\hat{H} = \hbar\omega_R\hat{a}^\dagger\hat{a} - E_J \cos[\omega_J t - \sqrt{\alpha}(\hat{a}^\dagger + \hat{a})], \quad (2)$$

up to the resonator zero-point energy. Note that ϕ_J is conjugate to the number N of Cooper pairs transferred through the JJ and \hat{H}_J is the sum of the operators $e^{\pm i\hat{\phi}_J}$ that increase or decrease N by one unit; as a consequence, \hat{H}_J couples Cooper pair transfer to photonic excitations in the resonator [7,15]. The Hamiltonian (2) shows that the strength of this coupling is given by α , which is the charge-radiation coupling constant [4] of our one-mode circuit, and plays the same role as the fine structure constant α_{QED} in atomic physics. This coupling results in inelastic Cooper pair tunneling and in a dc current flowing through the circuit in the vicinity of voltages V_k . At $\omega_J = k\omega_R + \delta_k$, the effective Hamiltonian obtained within the rotating-wave approximation takes the form [34,35]

$$\hat{H}_k = -\frac{E_J e^{-\alpha/2}}{2} \alpha^{k/2} [e^{-i\delta_k t} (i\hat{a}^\dagger)^k \hat{B}_k + \text{H.c.}], \quad (3)$$

where H.c. denotes Hermitian conjugation and

$$\hat{B}_k = \sum_{n=0}^{\infty} \frac{n!}{(n+k)!} L_n^{(k)}(\alpha) |n\rangle\langle n| \quad (4)$$

is a diagonal operator in the Fock state basis $\{|n\rangle\}$ involving the generalized Laguerre polynomials $L_n^{(k)}(\alpha)$ [35]. The Cooper pair translation operators $e^{\pm i\hat{\phi}_J}$ have thus been transformed into creation and annihilation operators $\hat{a}^{(\dagger)k}$ adding or removing bunches of k photons to or from the resonator. Under a constant voltage, a steady-state situation is reached, characterized by an average number of photons in the resonator, the occupation number $\langle n \rangle$: Cooper pairs tunnel across the JJ at a rate γ_k and produce photons in the resonator; these photons leak at an average rate $\Gamma_k = k\gamma_k = \kappa\langle n \rangle$ in the

a_{out} modes of the measurement line (see Fig. 4 in the Appendix A). This photon rate is expected to be proportional to the square of the prefactor $E_J e^{-\alpha/2} \alpha^{k/2}/2$ in Hamiltonian (3), and to also depend, through \hat{B}_k , on the actual photon distribution probability inside the resonator.

In the limit of vanishing E_J the situation is simpler since the resonator has time to empty before a new Cooper pair tunnels and a new bunch of k photons is emitted. The rate

$$\gamma_k = \frac{\Gamma_k}{k} = - \left(\frac{E_J}{\hbar\omega_R} \right)^2 \frac{\alpha^k e^{-\alpha}}{kk!} \frac{Q\omega_R}{1 + \left(\frac{2Q\delta_k}{k\omega_R} \right)^2} \quad (5)$$

is obtained in this case from a standard calculation of the Purcell relaxation rate for Hamiltonian (3), which holds when $\gamma_k \ll \kappa$, and coincides with the prediction of dynamical Coulomb blockade theory [22]. In this regime of well-separated tunnel events, the microwave radiation consists of separated bunches of k photons. This granularity of the energy flow is naturally measured by the photon Fano factor F_k , defined as the ratio of the variance to the mean number $\Gamma_k t$ of emitted photons during a time $t > \Gamma_k^{-1}$. Assuming a Poissonian electrical current with a Cooper pair Fano factor of 1, and k photons per Cooper pair crossing the circuit, one predicts $F_k = k$. Now, in the microwave domain, no wideband photon counters exist and the emitted photons cannot be counted during a given period of time. Instead, the field statistics can be characterized by the normalized second-order (intensity-intensity) correlation function,

$$g^{(2)}(\tau) = \frac{\langle \hat{a}_{\text{out}}^\dagger(0) \hat{a}_{\text{out}}^\dagger(\tau) \hat{a}_{\text{out}}(\tau) \hat{a}_{\text{out}}(0) \rangle}{\langle \hat{a}_{\text{out}}^\dagger \hat{a}_{\text{out}} \rangle^2}, \quad (6)$$

which can be interpreted as the probability for two photons separated by a delay τ to leak in the same electromagnetic mode. Then, F_k can be computed from $g^{(2)}$ [36] as

$$F_k = 1 + 2\Gamma_k \int_0^{+\infty} [g^{(2)}(\tau) - 1] d\tau. \quad (7)$$

In the strong brightness regime at large E_J , the resonator population feeds back to the emission dynamics [37]. A numerical integration of the evolution of the system under the influence of Hamiltonian (3) and radiative losses with rate κ is necessary to predict both the emission rate Γ_k and the Fano factor F_k .

III. IMPLEMENTATION

The α^k factor in Eq. (5) calls for a large value of α to favor the multiphoton emission beyond the already observed $k = 2$ case [7]. Standard on-chip microwave resonator designs yield a characteristic impedance smaller than the vacuum impedance $Z_V \simeq 377 \Omega$, with typically $\alpha \sim 0.05$. To approach $\alpha \sim 1$, we use a spiral coil resonator

[see Fig. 1(b)] etched in a 150-nm-thick niobium film sputtered onto a quartz substrate (low dielectric constant $\epsilon_r \simeq 3.8$), whereas the JJ is a superconducting quantum interference device (SQUID) with an E_J of a few μeV magnetically tunable down to almost zero. The resonator capacitance being the spurious capacitance to ground of its coil in parallel with the JJ capacitance, its resulting central frequency and characteristic impedance are $\nu_R = 4406 \text{ MHz}$ and $Z_R = 1.97 \text{ k}\Omega$, which corresponds to $\alpha = 0.96$.

The data reported here were collected over three different experimental runs by measuring a sample previously used to demonstrate photon antibunching at $k = 1$ [22]. Over these runs that extended over four years, the tunnel resistance of the SQUID increased from 220 to 330 k Ω due to aging, leading to a similar decrease of the maximum reachable E_J value. Runs 1 and 2 were performed in a dilution refrigerator (DR) with a liquid helium cryostat, whereas run 3 used a cryo-free DR with a pulse tube. As a result, the bias voltage noise was $\sim 4 \text{ nV}$ in run 2 and $\sim 80 \text{ nV}$ in run 3, which corresponds to Josephson frequency noises with standard deviations of about 2 and 38 MHz, respectively (see Appendix F). For all runs, the sample was placed in the same shielded sample holder, and was thermally anchored to the mixing chamber of the DR. The sample was connected through the same bias tee to a dc line with a filtered voltage divider, and to a 50 Ω microwave detection circuit. With such a low-impedance detection scheme, the quality factor Q of the resonator cannot be precisely controlled and has to be measured precisely *in situ* (see Appendix C; $Q = 36.6$ and 72 in runs 2 and 3). The detection line is made of a 90° hybrid coupler acting as a microwave beam splitter toward two nominally identical amplified lines 1 and 2 (see Appendix A). At room temperature, the signals $v_1(t)$ and $v_2(t)$ from the two lines were measured in different ways: in run 1, their powers are measured using two quadratic detectors, whereas in runs 2 and 3, they are bandpass filtered and down-converted to the 0–625 MHz frequency band using two mixers sharing the same local oscillator at $\nu_{\text{LO}} = 4.71 \text{ GHz}$. In this latter case, the two output quadratures are then digitized at 1.25 GSamples/s. The relevant correlation functions are then computed to obtain the emitted power spectral density, the total emitted power, the second-order coherence function $g^{(2)}(\tau)$, and the corresponding Fano factor F_k at the output of the resonator. As in Ref. [22], this two-line measurement setup *à la* Hanbury Brown and Twiss is a convenient way to remove the contribution of the technical noises from the determined quantities (see Appendix B).

IV. MEASURED AND SIMULATED EMITTED POWER

In the first experiment (run 1) we simply sweep the voltage V and integrate the received power over a bandwidth larger than the resonator one. We observe regularly

spaced peaks [see Fig. 1(c)] that correspond to the k -photon excitation mechanism described above at $V = V_k$, for $k = 1$ –5. In order to observe emission at such large values of k , we used the external magnetic field to tune our system to a large Josephson energy $E_J/h\nu_R \sim 0.1$ –0.2 (which could not be determined precisely due to the hysteretic magnetic behavior of the sample; see Appendix E). One notices in particular that the $k = 2$ and $k = 3$ peaks are stronger than the $k = 1$ peak, a situation that does not naturally occur in atomic physics because of the smallness of the fine structure constant. The last visible peak that appears below the voltage expected for $k = 6$ does not correspond to a multiple order resonance, and results from a spurious mode of the setup that could be strongly reduced in run 2.

In order to analyze more in depth the multiphoton emission process observed, the power spectral densities (PSDs) of the emitted radiation were measured in run 2, close to each V_k up to $k = 6$, and as a function of E_J in a range $E_J/h\nu_R = 0.01$ –0.142 (see Fig. 2). Spectra for the highest E_J are displayed in Fig. 2(a) and show a maximum brightness for $k = 3$. The applied bias voltages being slightly offset by δV_k , the emission peaks are frequency shifted from the resonator frequency ν_R by $\delta_k/2\pi = 2e\delta V_k/hk$. The spectral shapes are well fitted by Lorentzian peaks up to $k = 5$. The $k = 6$ peak is now clearly visible, but with a small parasitic contribution on its high-frequency side (which could be due to the emission of one photon in the resonator and another one in a 22.1 GHz spurious mode of the circuit).

We then compare the measured spectra with those predicted from simulations of the master equation of the circuit with Hamiltonian (3) and rate κ , without including the ~ 2 MHz Josephson frequency noise nor the detunings δ_k . These theoretical spectra are shifted by δ_k and superposed to the measured spectra in Fig. 2(a). At $k = 1$ the theoretical spectrum is close to a monochromatic line at the Josephson frequency, so that the width of the measured spectrum is almost entirely due to the bias voltage noise. At higher k , energy conservation only imposes the sum of the k -photon frequencies to be equal to the Josephson frequency, so that the emission width is larger. The simulated spectra have widths that vary with k in a nontrivial way, and reproduce reasonably well the measured spectra. The experimental emission peaks are also slightly widened by the noise.

The integral of the Lorentzian fit of a PSD yields the corresponding total photon flux Γ_k leaking out of the resonator. Note that the measured flux gives the resonator occupation $\langle n_k \rangle = \Gamma_k/\kappa$ because the resonator population decays dominantly by the photon emission into the measurement line. These photon fluxes are displayed as dots in Fig. 2(b), for 12 different values of the coil current and consequently of E_J . Unfortunately, the magnetic flux through the SQUID being hysteretic when ramping the coil current (see Appendix E), we had to use the following procedure to determine these E_J values and compare the

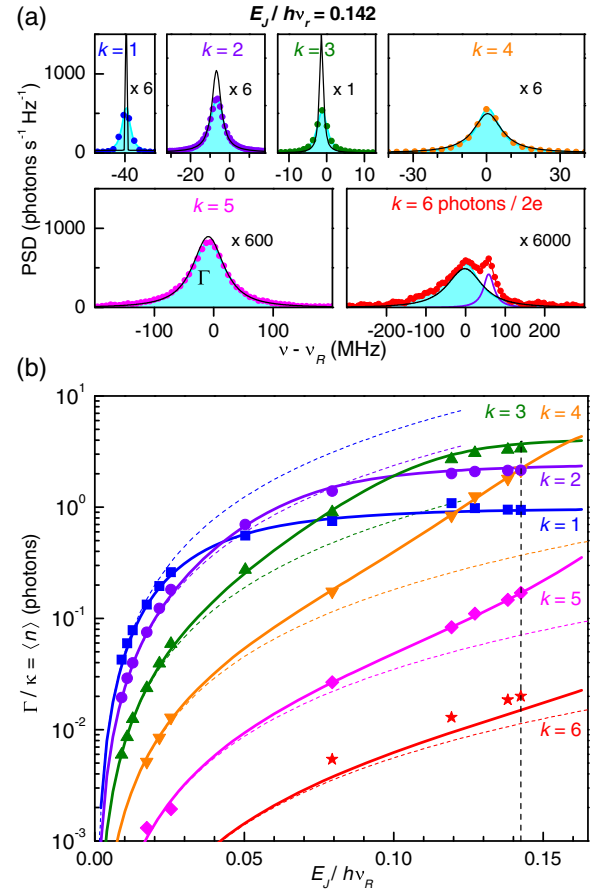


FIG. 2. Multiphoton emission spectra and emitted power for $k = 1$ –6. (run 2). (a) Examples of measured (dots) power spectral densities (PSD) taken at $E_J/h\nu_R \sim 0.142$ around the resonator frequency ν_R , for different bias voltages $V_k + \delta V_k$ corresponding to residual frequency detunings $\delta_k/2\pi = 2e\delta V_k/hk = -39.4, -6.0, -1.2, 1.4, -7.5, \text{ and } 0.8$ MHz for $k = 1, \dots, 6$. A vertical magnification factor with respect to the left axis scale is indicated for each peak. Cyan filled peaks are Lorentzian fits of the PSDs (for $k = 6$, a two-Lorentzian fit gives a second spurious mode in violet). The cyan areas are the photon rates Γ_k used for comparison with simulations in (b). Bare simulations of the discretized spectral densities at zero detuning (black solid lines) are shown (horizontally shifted) for comparison. (b) Measured (dots) and simulated (solid lines) reduced emission rates $\langle n \rangle = \Gamma_k/\kappa$ for $k = 1$ –6 and 12 different E_J values. Dashed curves represent the number of photons obtained from the Purcell rate γ_k of departure from the vacuum state (see text). Because of magnetic flux jumps in the SQUID, experimental E_J values were not precisely known and were fitted to minimize the difference between simulation and experiment in log scale (see text and Fig. 7 in Appendix E). No voltage noise is included in the simulation and no vertical scaling of the data is applied after calibration. The $\pm 5\%$ systematic relative uncertainty on calibration plus the uncertainty on k is about the symbol size. The vertical dashed line corresponds to the dataset in (a).

data to simulations: the six photon fluxes Γ_k are simulated over the full $E_J/h\nu_R = 0.01$ –0.15 range. The simulated curves are then used to fit the whole dataset with the 12 E_J values as fitting parameters. These fitted E_J are then

validated by the independently characterized hysteretic behavior of the SQUID (see Appendix E). The simulated and measured Γ_k match quantitatively over more than 3 orders of magnitude, with, however, a 25%–30% discrepancy for $k = 6$. The theoretical predictions of Eq. (5) in the weak brightness regime are also shown as dotted lines. They also account for the data at small E_J and occupation $\langle n \rangle$, but fail to predict the brightness increase when the resonator occupation differs significantly from zero and feeds back on the emission dynamics.

V. GRANULARITY OF THE MICROWAVE EMISSION

The microwave granularity was measured in run 3 for $k = 1$ –4, by computing the $g^{(2)}$ functions from the digitized demodulated signals v_1 and v_2 (see Appendix B), for six different values of E_J (see Fig. 9 in Appendix G). An example is also shown in Fig. 3(b). Because of the magnetic hysteresis of the SQUID already mentioned, these E_J values and their uncertainties are now inferred from the comparison of the measured average photon number $\langle n \rangle$ with simulations. The large ~ 80 nV voltage noise observed in run 3 now has to be included in the simulation (see Appendix H) for a quantitative agreement. The corresponding Fano factors are shown in Fig. 3(c) and compare reasonably well with numerical simulations. As expected, the simulated F_k tend toward k at vanishing brightness but depart significantly from it when E_J is increased. At the lowest E_J compatible with a reasonable measuring time (~ 72 h), we measure $F_{1,2,3,4} = 0.7 \pm 0.1, 1.8 \pm 0.1, 3.5 \pm 0.3, \text{ and } 4.5 \pm 0.6$, respectively, close to the expected bunch sizes $k = 1, 2, 3, \text{ and } 4$. This result, together with the quantitative understanding of the total emitted power, are the main results of the present work. This k granularity of the emission at low E_J means that the resonator is prepared in Fock state $|k\rangle$, at each Cooper pair tunneling event. Note that other circuit-QED devices can prepare such Fock states, but in a series of about k successive operations involving a superconducting qubit coupled resonantly [38] or dispersively [39] to a resonator. All these devices can thus be regarded as sources of k -photons multiplets.

Upon increasing E_J , the Fano factors show a complex behavior with a dip for $k = 1$ and a peak-dip structure for $k > 1$ [see Fig. 3(c)], although the increase in the resonator occupation $\langle n \rangle \lesssim 1$ remains moderate [see Fig. 3(a)]. In essence (see Appendix I), these variations are a consequence of two competing nonlinear effects. First, at moderate occupation, the k -parametric term $\sim (\hat{a}^\dagger)^k + \hat{a}^k$ of Hamiltonian (3) has matrix elements increasing rapidly with the number n of photons. This results in an emission stimulated by the photons already present in the resonator, an enhanced emission rate, and a superlinear Fano factor $F_k > k$ that indicates an additional bunching of the k -photon multiplets [14,15,40]. Second, however, at larger E_J and occupation $\langle n \rangle$, the Josephson nonlinearity encoded in

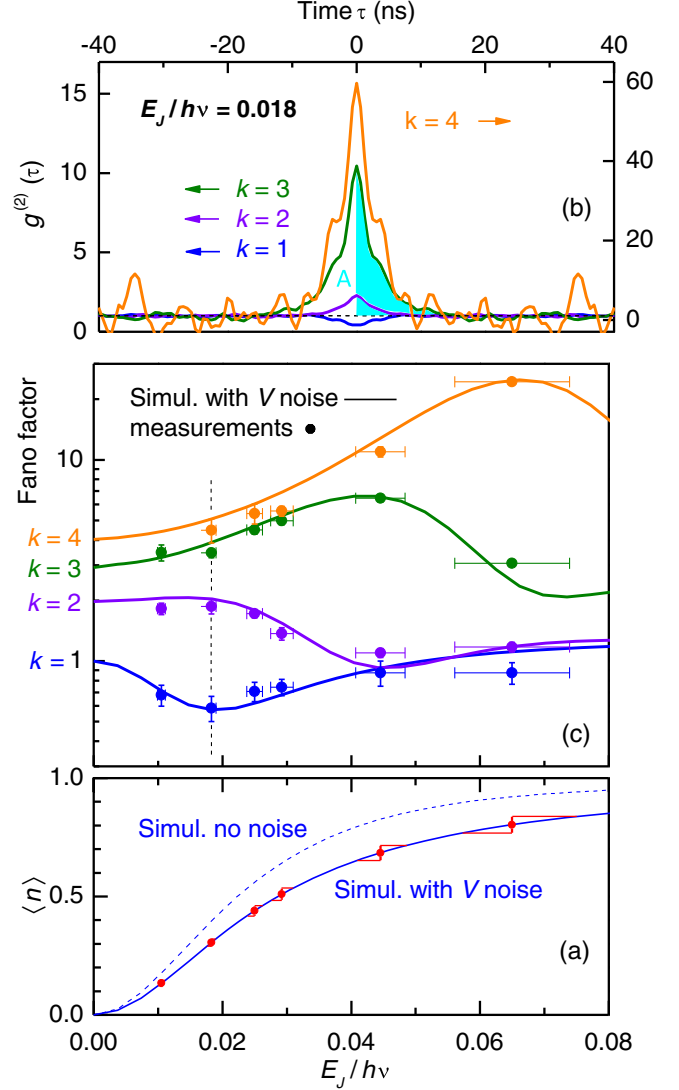


FIG. 3. Noise statistics and Fano factors of the leaking microwave (run 3). (a) Calibration of the E_J values by placing the measured $\langle n \rangle$ (dots) on a simulation of the $\langle n \rangle(E_J)$ curve including the effect of the observed voltage noise (solid line). Simulation with a noiseless bias voltage (dashed line) is also shown for comparison. The uncertainty on $\langle n \rangle$ (vertical error bars) yields the uncertainty on E_J (horizontal error bars). (b) Example of a set of $g^{(2)}$ functions measured at a small $E_J/\hbar\omega_R = 0.018$. The area between $g^{(2)}$ and 1, integrated over the 0–40 ns time interval (shown in cyan for $k = 3$) enters the Fano factor of (c). (c) Experimental Fano factors (dots) and simulated Fano factors including voltage noise (solid curves). Horizontal error bars correspond to those of (a), whereas vertical error bars correspond to ± 2 standard deviations. The vertical dashed line corresponds to the raw data of (a).

\hat{B}_k reduces strongly the drive strength, at different occupation levels that depend on k . For $k = 1$, this last effect even leads to a strong antibunching (see Ref. [22] and $g^{(2)}(0) < 1$ in Fig. 9 of Appendix G).

Finally, beyond the k granularity of the photon emission, an interesting point to note is the quantum nature of the

resonator field \hat{a} and radiated fields \hat{a}_{out} : as the emission is similar to a k -photon spontaneous parametric down-conversion [see the \hat{B}_k -modified $(\hat{a}^\dagger)^k + \hat{a}^k$ term in Hamiltonian (3)], the Wigner functions of the fields are expected to be non-Gaussian and squeezed with a k -fold symmetry, as measured recently in Ref. [3] for $k = 3$. Our experiment was designed to measure photon statistics and does not permit measurement of these Wigner functions. However, we show an example of simulated Wigner functions in Appendix J to motivate their measurement in the future.

VI. CONCLUSION

In conclusion, our work shows that a high-impedance resonator in series with a voltage-biased Josephson junction produces, at particular voltages V_k , bunches of $k = 1, \dots, 6$ photons per Cooper pair tunneling across the Josephson junction, with a brightness quantitatively understood. By measuring both the emitted power and the Fano factor of the system, we have shown that the photons are indeed emitted as multiplets in a single event. Note that a similar emission process was also recently observed in a richer multimode environment [33]. Our simple system provides an interesting test bench for quantum optics experiments in the strong charge-radiation coupling regime provided by the high-impedance, moreover in a steady-state out-of-equilibrium situation imposed by the voltage source, a regime far from atomic physics. Beyond illustrating and clarifying a new regime of quantum optics, such simple photon sources complete the quantum microwaves toolbox.

ACKNOWLEDGMENTS

We gratefully acknowledge stimulating discussions within the Quantronics and Nanoelectronics groups and with K. Mølmer and A. Armour, as well as the technical help from P. Jacques. This work received funding from the European Research Council (Horizon 2020/ERC Grant Agreement No. 639039 and NSECPROBE), from the French LabEx PALM (ANR-10-LABX-0039-PALM), from the French ANR (contracts GEARED ANR-14-CE26-0018-01 and SIMCIRCUIT ANR-18-CE47-0014-01), from the German-French ANR/DFG Grant JosePhScharli, from IQST and the German Science Foundation (AN336/13-1). This article concludes a series of works on microwave quantum photonics utilizing voltage-biased Josephson circuits, that our colleague and friend Fabien Portier had inspired and led until his passing on December 2, 2020.

APPENDIX A: COMPLETE EXPERIMENTAL SETUP

Figure 4 presents the electrical schematics of our experimental bias and detection circuits. As explained in the main text, our sample is anchored at the bottom plate of a dilution refrigerator and connected to the measurement

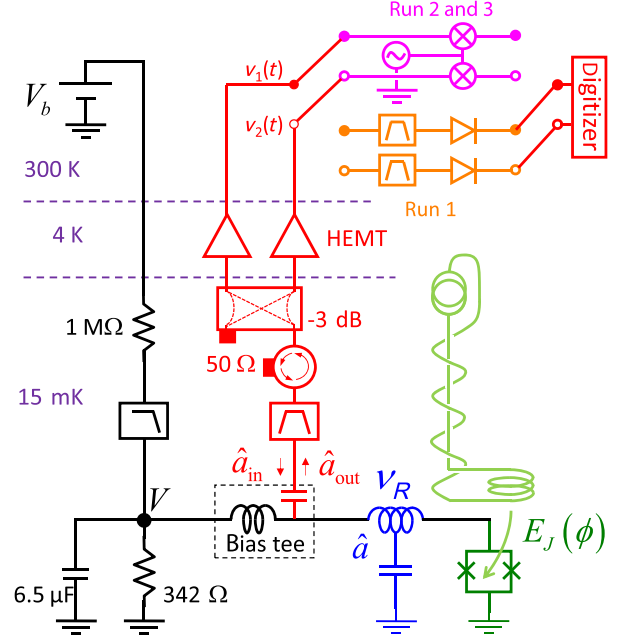


FIG. 4. Experimental setup. Schematics of the whole measurement circuit used in the different experimental runs (see text).

chain. The black subcircuit with a bias tee is used to apply a finite bias to the junction (dark green), which generates the emission of photons into the resonator (blue). An external magnetic coil (light green) threads a magnetic flux ϕ through the SQUID to tune its Josephson energy E_J . The signal leaking from the resonator (mode a_{out}) goes through a bandpass filter and a circulator before being split over two lines in a Hanbury Brown–Twiss-like setup and then amplified (red). Depending on the experimental run, we either send each signal to a bandpass filter and a diode (in orange, run 1) or heterodyne them (purple, runs 2 and 3), before digitizing them.

APPENDIX B: DETERMINATION OF SPECTRAL DENSITIES, TOTAL POWERS, AND $g^{(2)}$ FUNCTIONS (RUNS 2 AND 3)

1. Model for the detection chain

We describe here the same procedure as the one given in the Supplemental Material of Ref. [22].

The input-output formalism links the resonator operator \hat{a} to the ingoing and outgoing transmission line operators \hat{a}_{in} , \hat{a}_{out} by $\sqrt{\kappa}\hat{a}(t) = \hat{a}_{\text{in}}(t) + \hat{a}_{\text{out}}(t)$, with $\kappa = \omega_R/Q$ the energy leak rate. In our experimental setup, \hat{a}_{in} describes the thermal radiation coming from the 50Ω load on the isolator closest to the sample. Because this load is thermalized at $15 \text{ mK} \ll \hbar\omega_R/k_B$, the modes impinging onto the resonator can be considered in the ground state and the contribution of \hat{a}_{in} to all the correlation functions vanishes. We thus take \hat{a}_{out} to be an exact image of \hat{a} , and all their normalized correlation functions as being equal.

As described in the previous Appendix, the emitted signal is split between two detection chains, filtered, amplified, and mixed with a local oscillator before digitization. The beam splitter is implemented as a hybrid coupler with a cold 50Ω load on its fourth port, and acts as an “amplifier” of gain $1/2$, adding to the signal a noise mode \hat{h}_{bs} in the vacuum state. The different amplifying stages are summed up into one effective amplifier for each channel, with respective noise temperatures $T_N^{(1)} = 13.5$ K and $T_N^{(2)} = 14.1$ K for runs 1 and 2 and $T_N^{(1)} = 8.12$ K and $T_N^{(2)} = 6.16$ K for run 3. The mixer used for heterodyning the signals also adds to them at least the vacuum noise.

The last step is the linear detection of the voltage $v_i(t)$ on channel i by the acquisition card. It is classical and does not have to be modeled at the quantum level. After digitization, we process chunks of signal of length 1024 samples to compute the analytical signal $S_i(t) = v_i(t) + H(v_i(t))$, where H is here the discrete Hilbert transform. Because computing the analytical signal $S_i(t)$ from the heterodyned $v_i(t)$ is equivalent to measuring its two quadratures, which are noncommuting observables, quantum mechanics imposes an additional noise mode. We sum this digitization noise and the heterodyned noise into a single demodulation noise.

Ultimately, we record measurements of $\hat{S}_1(t)$ and $\hat{S}_2(t)$, with $\hat{S}_i \propto \hat{a}_i + \hat{h}_i^\dagger$ and \hat{h}_i an effective thermal noise summing the different detection step contributions (in practice, the dominant noise contribution stems from the amplifiers closest to the sample). Note that $\hat{a}_i(t) \propto \hat{a}_{\text{out}}(t - \tau_i)$ with τ_i the propagation time on channel i , and that the signal model described above is valid only within the bandpass of the filters.

2. Computing correlations (runs 2 and 3)

For each chunk of signal recorded on line i we compute a chunk of $S_i(t)$ of the same length, 1024. We then compute the desired correlation functions as

$$C_{X,Y}(\tau) = \langle X^*(t)Y(t+\tau) \rangle = F^{-1}[F(X)^*F(Y)],$$

where $\langle \dots \rangle$ stands for the average over the length of the chunk and F is the discrete Fourier transform. Finally, we average the correlation functions from all the chunks and store this result for further postprocessing.

To illustrate how we reconstruct the information on \hat{a} from S_1 and S_2 , let us consider the first-order coherence function $g^{(1)}(\tau) = \langle \hat{a}^\dagger(t)\hat{a}(t+\tau) \rangle / \langle \hat{a}^\dagger\hat{a} \rangle$. We start with the product

$$\begin{aligned} S^*(t)S(t+\tau) &\propto \hat{a}^\dagger(t)\hat{a}(t+\tau) + \hat{h}(t)\hat{h}^\dagger(t+\tau) \\ &+ \hat{a}^\dagger(t)\hat{h}^\dagger(t+\tau) + \hat{h}(t)\hat{a}(t+\tau) \end{aligned}$$

on a single line, i.e., with S being either S_1 or S_2 . Then, we consider that the noise added by an amplifier cannot be

affected by the state of the resonator, so that \hat{a} and \hat{h} are independent and thus uncorrelated; hence,

$$\langle \hat{a}(\tau)\hat{h}(t+\tau) \rangle = \langle \hat{a}(\tau) \rangle \langle \hat{h}(t+\tau) \rangle = 0,$$

as there is no phase coherence in the thermal noise ($\langle \hat{h} \rangle = 0$). We thus have

$$\langle S^*(t)S(t+\tau) \rangle \propto \langle \hat{a}^\dagger(t)\hat{a}(t+\tau) \rangle + \langle \hat{h}(t)\hat{h}^\dagger(t+\tau) \rangle.$$

Hence, at zero bias voltage $V = 0$ (the so-called *off* configuration),

$$\langle S^*(t)S(t+\tau) \rangle_{\text{off}} \propto \langle \hat{h}(t)\hat{h}^\dagger(t+\tau) \rangle,$$

whereas at the finite voltage V for the multiphoton emission (so-called *on* configuration),

$$\langle S^*(t)S(t+\tau) \rangle_{\text{on}} \propto \langle \hat{a}^\dagger(t)\hat{a}(t+\tau) \rangle + \langle S^*(t)S(t+\tau) \rangle_{\text{off}}.$$

Consequently,

$$g^{(1)}(\tau) = \frac{\langle S^*(t)S(t+\tau) \rangle_{\text{on}} - \langle S^*(t)S(t+\tau) \rangle_{\text{off}}}{\langle S^*S \rangle_{\text{on}} - \langle S^*S \rangle_{\text{off}}}.$$

Now, as we are considering states of the resonator with at most a few photons, we typically have $\langle S^*S \rangle_{\text{off}} \simeq \langle S^*S \rangle_{\text{on}} \gg \langle S^*S \rangle_{\text{on}} - \langle S^*S \rangle_{\text{off}}$. From there, any small fluctuation of the gain of the detection chain or of the noise temperature during the experiment reduces greatly the contrast on $g^{(1)}(\tau)$. We thus rely on the cross-correlation $X(\tau) = \langle S_1^*(t)S_2(t+\tau) \rangle$ on the two lines rather than on the previous autocorrelation on one of them. (Note that due to a residual cross talk between the two channels, this cross-correlation averages to a finite value even in the off position, but which is 60 dB lower than the autocorrelation of each channel). We hence use

$$g^{(1)}(\tau) = \frac{X(\tau)_{\text{on}} - X(\tau)_{\text{off}}}{X(0)_{\text{on}} - X(0)_{\text{off}}}.$$

A similar treatment allows us to compute $g^{(2)}(\tau)$ with slightly more complex calculations. The classical Hanbury Brown–Twiss experiment correlates the signal power over the two channels, i.e., extracts $g^{(2)}(\tau)$ from $\langle S_1^*S_1(t)S_2^*S_2(t+\tau) \rangle$. The off value of this correlator is once again much bigger than the relevant information of the *on-off* part, and any drift of the amplifiers would blur the averaged value of $g^{(2)}(\tau)$. This is why we use $C(t) = S_1^*(t)S_2(t)$ instead of $S_i^*(t)S_i(t)$ as a measure of the instantaneous power emitted by the sample, provided that the time delay between the two detection lines is calibrated and compensated for. We then have

$$\begin{aligned}
g^{(2)}(\tau) &= \frac{\langle C(t)C(t+\tau) \rangle_{\text{on}} - \langle C(t)C(t+\tau) \rangle_{\text{off}}}{(\langle C \rangle_{\text{on}} - \langle C \rangle_{\text{off}})^2} \\
&- 2 \frac{\langle C \rangle_{\text{off}}}{\langle C \rangle_{\text{on}} - \langle C \rangle_{\text{off}}} \frac{[X(\tau)_{\text{on}} - X(\tau)_{\text{off}}]X(-\tau)_{\text{off}}}{(\langle C \rangle_{\text{on}} - \langle C \rangle_{\text{off}})^2} \\
&- \frac{[X(-\tau)_{\text{on}} - X(-\tau)_{\text{off}}]X(\tau)_{\text{off}}}{(\langle C \rangle_{\text{on}} - \langle C \rangle_{\text{off}})^2}, \quad (\text{B1})
\end{aligned}$$

where $\langle C \rangle$ stands for $\langle C(t) \rangle$.

3. Computing power spectral densities, total emitted powers, and Fano factors from correlations

From the raw cross-correlation $C(\nu)$ [Fourier transform of $C(t)$], we compute the normalized emitted power spectral density:

$$\text{PSD}(\nu) = \frac{C(\nu)_{\text{on}} - C(\nu)_{\text{off}}}{C(\nu)_{\text{off}}}.$$

The photon emission rate,

$$\Gamma = \frac{k_B T_N}{h} \int_{\text{BW}} \frac{\text{PSD}(\nu)}{\nu} d\nu,$$

is then obtained by integrating the PSD over the bandwidth (BW) of the resonator, with $T_N \sim 7.5$ K the effective noise temperature of the cross-correlated signal. We then use this photon emission rate Γ and the fully corrected $g^{(2)}(\tau)$ described above to compute the Fano factors:

$$F_k = 1 + 2\Gamma_k \int_0^{+\infty} [1 - g^{(2)}(\tau)] d\tau.$$

The experimental $g^{(2)}(\tau)$ and the estimation of the error on F_k are presented in Appendix G.

APPENDIX C: RESONATOR PARAMETER DETERMINATION

Both runs 2 and 3 started with the determination of the resonator parameters. This was done by recording the PSD for many values of the bias voltage V around $V_{k=1}$ (that is many values of the Josephson frequency ν_J). The total emitted power was then computed as indicated in the previous Appendix. This power being proportional to the real part of the resonator impedance $\text{Re}[Z(\nu_J)]$, plotting it as a function of the central frequency ν_J of each spectrum reconstructs the resonator line shown in Fig. 5 (for run 3). Fitting the resonator line by a Lorentzian peak yields the central frequency of the resonator $\nu_R = 4406.75 \pm 0.25$ MHz and a FWHM of 61.05 ± 1.2 MHz corresponding to a quality factor $Q = 72 \pm 1.4$ (run 3). The same procedure yields $Q = 36.6 \pm 0.7$ for run 2.

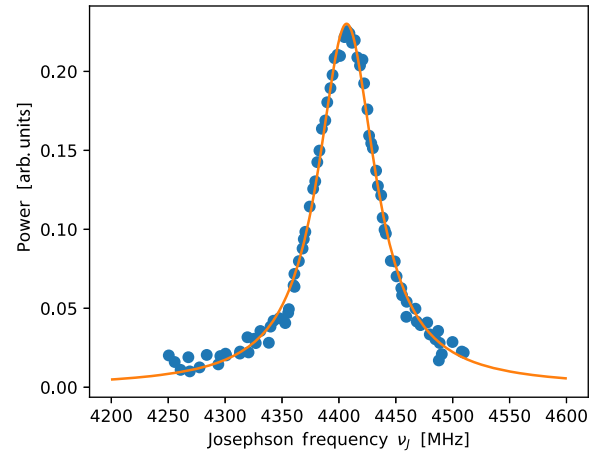


FIG. 5. Characterization of the resonator. Measured total emitted power (dots) as a function of the central frequency of the emitted spectrum. The orange line is a Lorentzian fit yielding the resonator frequency $\nu_R = 4406.7 \pm 0.25$ MHz and quality factor $Q = 72 \pm 1.4$ (run 3).

APPENDIX D: ESTIMATION OF THE MAXIMUM JOSEPHSON ENERGY (RUN 3)

In order to estimate the absolute maximal Josephson energy of our SQUID, we measure the emission at $k = 1$ at a bias voltage corresponding to $\nu_J = 5.15 \pm 0.01$ GHz (on the high-frequency tail of the resonance), in order to maintain a low brightness and have a total emission rate given by

$$\Gamma = \frac{2\pi^2 (E_J^*)^2 \text{Re}[Z(\nu_J)]}{\hbar^2 \nu_J R_K}, \quad (\text{D1})$$

where $R_K = h/e^2$ is the resistance quantum and E_J^* the effective Josephson energy of the SQUID renormalized by the phase fluctuations of its environment. We record Γ as a function of the magnetic field [see Fig. 6(b)] by sweeping the coil voltage in a single direction, extremely slowly and with very small steps, in order to avoid the lag and hysteresis mentioned in the main text and documented in the next Appendix. As E_J^* varies as the absolute value of a cosine function of the magnetic field, Γ varies sinusoidally as expected, and a sinusoidal fit yields a precise value of the maximum emission rate Γ_{max} . To eliminate the unknown $\text{Re}[Z(\nu_J)]$ in Eq. (D1) and obtain $E_{J,\text{max}}^*$, we also measure the power spectral density $S(\nu)$ of the shot noise emitted when biasing the circuit at a voltage V well above twice the superconducting gap voltage (~ 200 μ V). We then divide Γ_{max} by the derivative

$$\frac{dS(\nu)}{dV} = 2e \frac{\text{Re}[Z(\nu)]}{R_N}, \quad (\text{D2})$$

at frequency ν_J [see Fig. 6(a)], with R_N the normal resistance of the SQUID that we estimate to be 335 ± 6 k Ω in run 3. The Josephson energy is thus simply given by

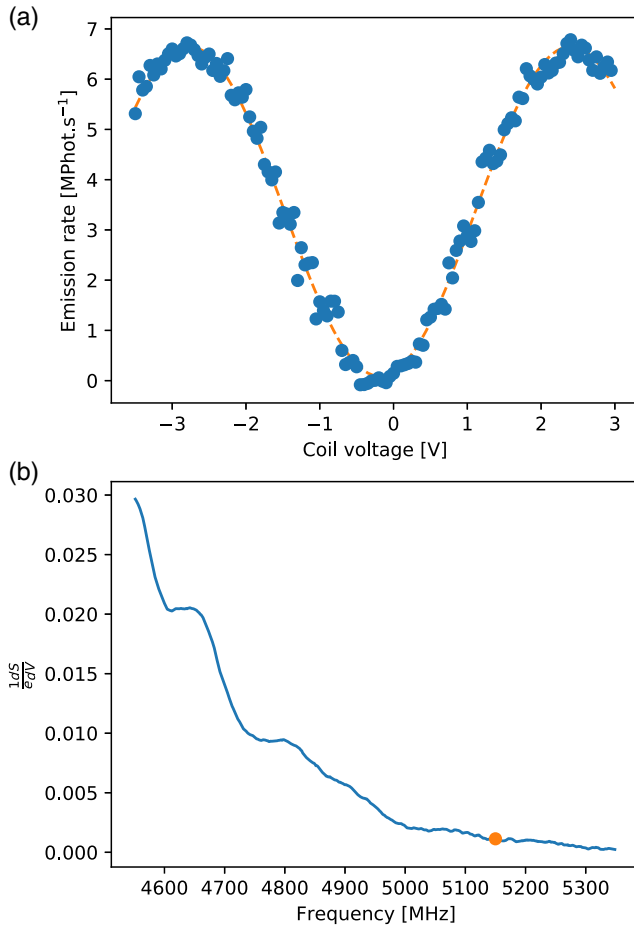


FIG. 6. Calibration of E_J via the field dependence of the emission. (a) Photon emission rate Γ expressed in mega photons per second measured (dots) as a function of the voltage applied to the coil, recorded at $\nu_J = 5.15 \pm 0.01$ GHz, far from the resonance frequency of the resonator. The dashed orange line is a sinusoidal fit. (b) Derivative of the shot-noise signal as a function of the frequency. The orange dot shows the point at ν_J used for dividing Γ (see text).

$$E_J^{*2} = \frac{\Gamma_{\max}}{dS/dV} \frac{eh^2\nu R_K}{\pi^2 R_N}.$$

We find $E_{J,\max}^* = 1.01 \pm 0.02 \mu\text{eV}$, to be compared to the Ambegaokar-Baratoff value $E_{J,\max}^{\text{AB}} = 1.73 \pm 3 \mu\text{eV}$, which indicates a renormalization factor of 0.583 in perfect agreement with our estimate of 0.587 (see Supplemental Material of Ref. [22] for the method).

APPENDIX E: HYSTERETIC MAGNETIC BEHAVIOR OF THE SQUID AND FITTED E_J VALUES (RUN 2)

As is the case for many Josephson devices, our sample suffers from the presence of magnetic vortices trapped in the superconducting electrodes in the vicinity of the SQUID. These vortices add a contribution to the external

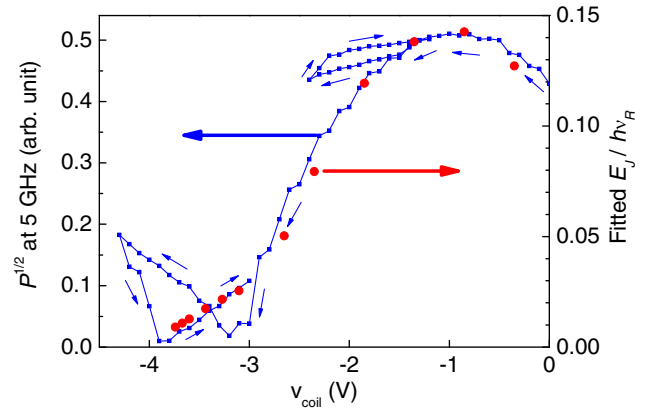


FIG. 7. Magnetic hysteresis and fitted E_J values. Square root of the emitted power \sqrt{P} at 5 GHz (blue points, left axis) versus applied coil voltage v_{coil} , and fitted E_J values (red, right axis) presented in Fig. 2 of the main text. A relative vertical scaling is applied to compare the two datasets.

magnetic field applied by the coil. As the coil field is ramped, the vortices can move and induce jumping or lagging of the effective flux experienced by the SQUID loop. Because the effective Josephson energy depends on this effective flux, its determination is problematic.

However, as explained in the previous Appendix, because the microwave emission is simply proportional to the square of the Josephson energy E_J in the low occupation limit, E_J variations can be followed from the measured emitted power when the bias voltage (or equivalently the Josephson frequency ν_J) is tuned far on the tail of the resonator resonance. Figure 7 shows a record of the square root of the emitted power \sqrt{P} for $\nu_J = 5$ GHz, when sweeping back and forth the magnetic field along a particular path indicated by the blue arrows: starting from $V = 0$ V, the voltage v_{coil} applied to the coil circuit goes down to -2.5 V, increases to -1.5 V, goes all the way down to -4.2 V, and finally reincreases to -3 V: a hysteretic emission is observed with lagging in both directions. To check that the E_J values fitted in run 2 make sense and are valid, we plot them as a function of v_{coil} and apply a relative vertical scaling to compare them to \sqrt{P} . The fitted E_J values fall on the recorded trajectory for the emission, which shows that they are consistent with the chosen v_{coil} values.

APPENDIX F: BIAS VOLTAGE NOISE

The fridge setups with which we performed our experiments presented a bias voltage noise with a standard deviation of about 4 nV in runs 1 and 2 and 80 nV in run 3. This transcribes into a Josephson frequency noise and a finite emission width (at $k = 1$) of less than 2 MHz and about 38 MHz, respectively, to be compared to the resonator linewidths of about 120 and 60 MHz, respectively. Consequently, we could neglect this noise in our

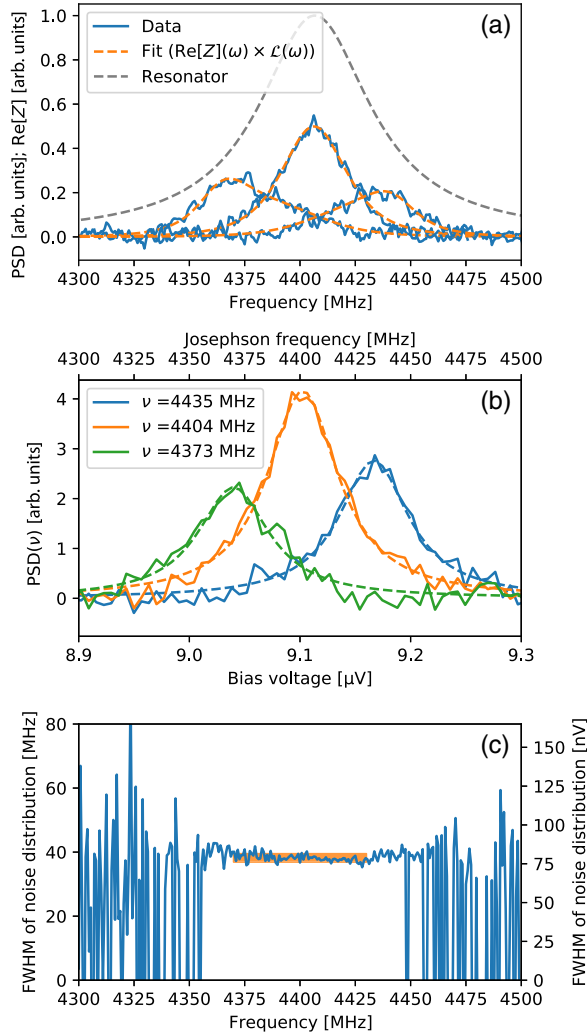


FIG. 8. Fitting of the voltage noise. (a) Example of three measured PSD of emission (blue lines) taken at various voltage biases, below, at, and above the resonator central frequency, as well as their fit (orange) by a product of two Lorentzian lines (see text). The resonator line shape (dashed gray line) is superposed to allow the reader to better locate the bias values. (b) Three examples of emitted power P (solid lines) taken at fixed frequencies ν as a function of the bias voltage V , as well as their Lorentzian fit (dashed lines). (c) FWHM extracted from many $P(V)$ curves as those shown in (b), on a dense bias grid. The orange bar shows the window used to compute the mean value of the emission width and its height indicates the corresponding standard deviation.

analysis for run 2, but had to take it into account for run 3. Indeed, when the circuit is biased at $V_0 = h\nu_{J_0}/2e$, the power spectral density at a given instant and at a frequency ν around ν_{J_0} is proportional to the product of the impedance of the resonator at that frequency ν by the probability to produce a photon at frequency $\nu = \nu_{J_0} + 2e\delta V/h$:

$$\text{PSD}(\nu) \propto \text{Re}[Z(\nu)] \times P(h\nu_{J_0} + 2e\delta V),$$

with δV the noise voltage at that instant.

In the case of a purely thermal noise with Gaussian statistics, one would assume the PSD at $k = 1$ to be the product of the Lorentzian shape of the resonator determined in Appendix C, centered on ν_R , by a Gaussian centered on ν_{J_0} . However, fitting the measured PSD revealed that also using a Lorentzian shape \mathcal{L} for the noise distribution yields better results [see Fig. 8(a)].

Now considering the emission at fixed frequency ν as a function of the bias voltage V (or ν_J) allows us to measure more directly the noise distribution [see the three examples of Fig. 8(b)], as the impedance $Z(\nu)$ becomes a simple multiplicative constant to a V -dependent line shape. Once again, a Lorentzian fit is in better agreement with the experimental data than a Gaussian. Figure 8(c) shows the FWHM of the noise distribution (expressed in frequency units), measured in this way on many curves at different biases: its value over a window centered on the resonator is 38.2 ± 1.3 MHz.

APPENDIX G: SET OF MEASURED $g^{(2)}$ FUNCTIONS AND FANO FACTORS (RUN 3)

Figure 9 presents the full set of $g^{(2)}(\tau)$ data, shown both for short and long times. Antibunching of the $k = 1$ case can be observed in the dip of $g^{(2)}(\tau)$ for $k = 1$ at all E_J values, as well as in the data taken at strong $E_J/h\nu = 0.045$ and 0.065 , for $k = 2$. We extract $F(k, E_J)$ by integrating $g^{(2)}(\tau)$ according to

$$F_k = 1 + 2\Gamma_k \int_0^{+\infty} [1 - g^{(2)}(\tau)] d\tau, \quad (\text{G1})$$

over the 40 ns time window shown in the left-hand panels of Fig. 9. The relative Fano factor uncertainty is determined by the standard deviation σ of $g^{(2)}$ measured at long time (right-hand panels) and the total number N of integrated points: $\Delta F_k/F_k = (1 - 1/F_k)(\Delta\Gamma_k/\Gamma_k + 2\Gamma_k\sqrt{N}\sigma/F_k)$.

APPENDIX H: INCLUDING THE EFFECTS OF VOLTAGE NOISE IN QUANTUM NUMERICAL SIMULATIONS

This Appendix describes how fluctuations of the bias voltage affect the dynamics of a Josephson-photonics system and how they can be accounted for in a simulation of measured observables. Obviously, all observables discussed here, from the resonator occupation and emitted power to correlation functions and Fano factors, depend on the detuning from the voltage matching condition, $2eV = k\hbar\omega$, of the k -photon resonance. Examples are the measured emitted power in Fig. 1(c) of the main text, or the simulated results in Fig. 10, which show the unnormalized correlation function $G^{(2)}(\tau) = \langle n \rangle^2 \times g^{(2)}(\tau)$ with the dependence of $G^{(2)}(\tau \rightarrow \infty) = \langle n \rangle^2$ on the detuning illustrated in the right-hand panel. In an experiment, even if the mean voltage is tuned to resonance,

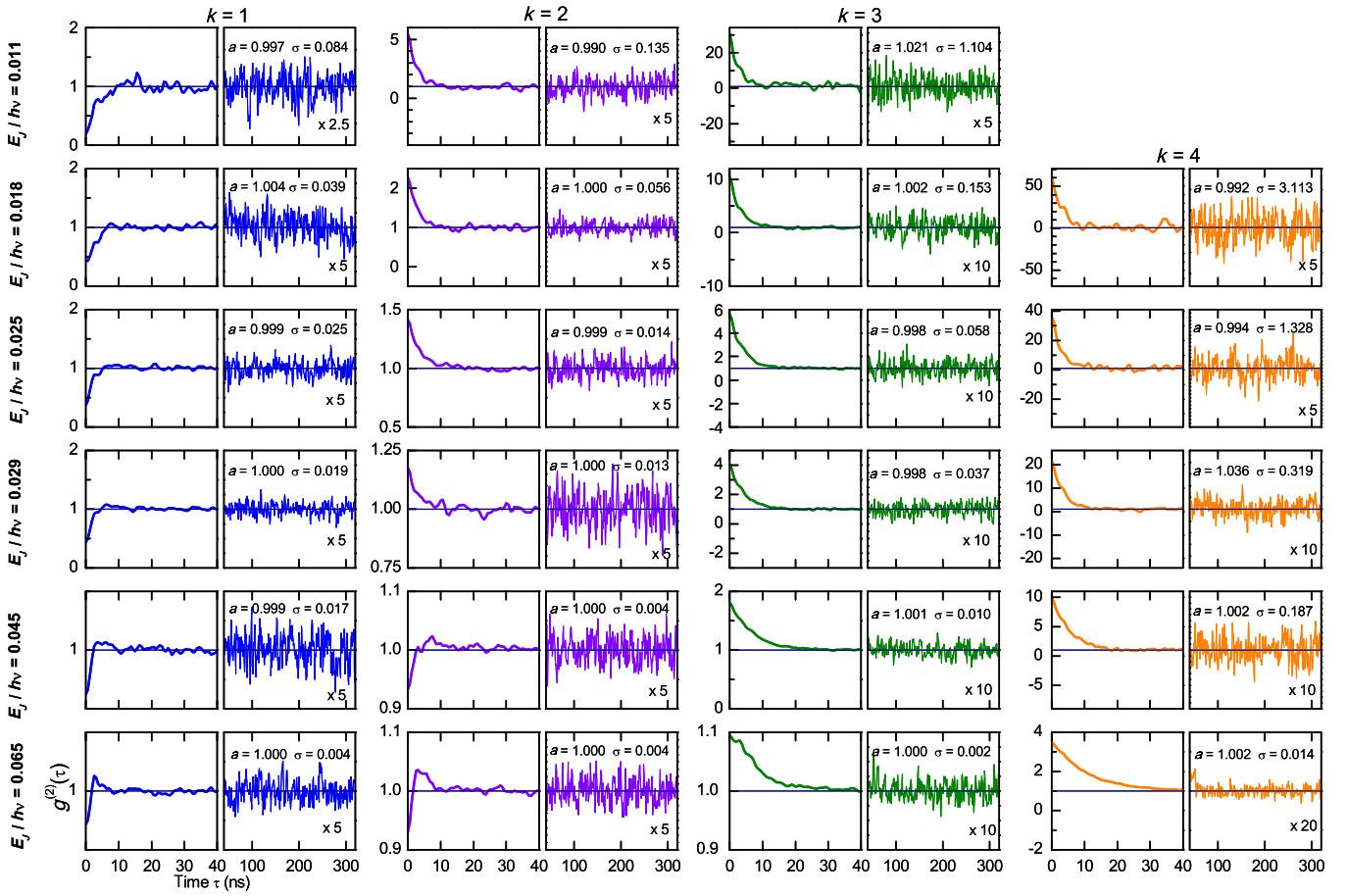


FIG. 9. Function $g^{(2)}(\tau)$ for various values of k and E_J . Raw experimental measurement of $g^{(2)}(\tau)$ from $k = 1$ to $k = 4$ (from left to right) and for $E_J/h\nu_r = \{0.011, 0.018, 0.025, 0.029, 0.045, 0.065\}$. The left-hand panel each panel pair presents the short time variation of g^2 while the right-hand panel presents the noise on the measured $g^{(2)}(\tau)$ fluctuating around 1 at long time. A vertical multiplication factor is indicated in these right-hand panels together with the average value a and the standard deviation σ of the noise.

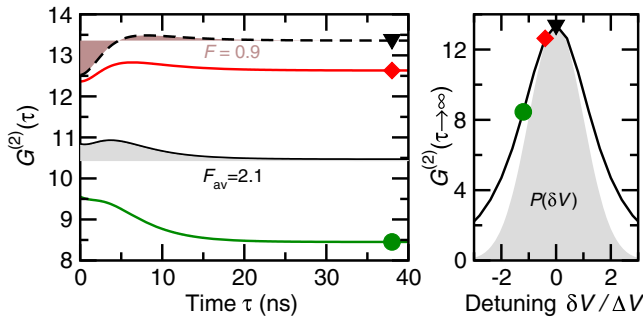


FIG. 10. Effects of voltage noise on the correlation function $G^{(2)}(\tau)$ are simulated by averaging over a Gaussian normal distribution $P(\delta V/\Delta V)$ (gray shaded in the right-hand panel) with the variance extracted from experiment as described in Sec. VIC. The unnormalized correlation functions $G^{(2)}(\tau)$ for three detunings (0, 0.2, and $0.4\Delta V$; see markers) are shown in the left-hand panel, together with the averaged result (black). The areas under the curves (shaded in the left-hand panel) enter the Fano factor according to Eq. (4) of the main text (other parameters are $k = 3$, $E_J = 0.9E_J^{\text{sat}} = 0.07/h\nu$).

voltage fluctuations will let the system explore the effects of such detuning. Voltage fluctuations are always present and have been carefully measured and characterized for the various runs of our experiments (see Appendix F). The typical size of fluctuations has been determined and is used to scale the voltage in the right-hand panel of Fig. 10. In fact, that typical size (in run 3) is not small, so that there is a substantial effect on the measured observables for typical fluctuations ΔV , as shown by the markers in Fig. 10, right, indicating detunings of 0, 0.2, and $0.4\Delta V$.

To account for the main effects of voltage fluctuations, one can assume that they are of thermal origin and of classical nature. While fluctuations are much slower than the excitation and leaking dynamics of the resonator, the averaging time over which measurements are assembled is much longer. In this quasistatic case, voltage fluctuations can be accounted for by averaging over a distribution of detunings. Assuming a classical noise model, we chose a Gaussian distribution. This noise model has been successfully used to prove and characterize entanglement of a two-resonator Josephson-photonics setup in Ref. [31], but

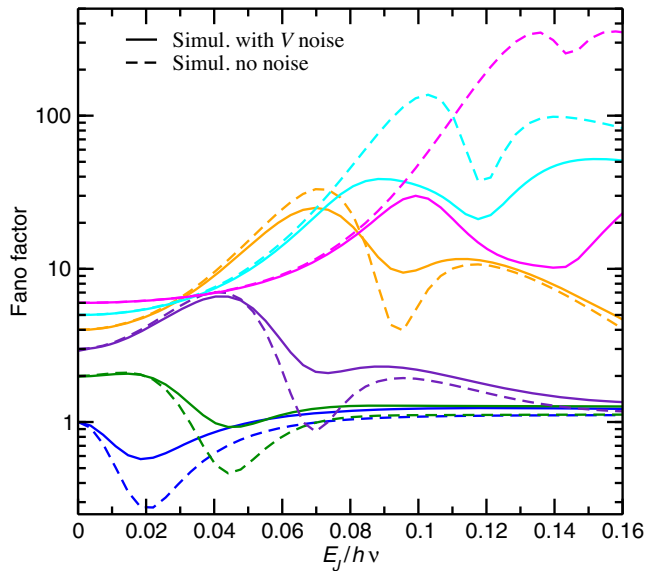


FIG. 11. Effects of voltage noise on the Fano factor in the weak driving limit. Dependence of the Fano factor on the effective driving strength $E_J/h\nu$ for the resonances $k = 1, 2, \dots, 6$ simulated (for zero nominal detuning) without noise (dashed lines), and including noise (solid lines) as described by Fig. 10).

different or refined methods (see, e.g., the Supplemental Material of Ref. [37]) are also possible.

We find that voltage noise has a substantial effect in our experiment. This can be seen already on mean observables, such as the mean number of photons in the resonator $\langle n \rangle$ [cf. Fig. 3(a) of the main text], but also on correlation functions (left-hand panel of Fig. 10) and on the Fano factor; see Fig. 11. The left-hand panel of Fig. 10 highlights a situation where that effect is very pronounced. As may be expected, this happens around the transition points of the semiclassical results discussed in Appendix I (which, in fact, show nonanalyticity only for the resonant case). Shown are the (unnormalized) correlation functions $G^{(2)}(\tau)$ for the three values of detunings indicated in the right-hand panel, as well as the result of averaging $G^{(2)}(\tau)$ over the distribution $P(\delta V)$, shown shaded in the right-hand panel. The averaging completely changes the time dependence of $G^{(2)}(\tau)$, and can even result in a super-Poissonian Fano factor, $F_{\text{av}} > 1$, where the noiseless resonant Fano factor would be sub-Poissonian, $F < 1$, represented by the shaded (positive and negative) areas and cf. Fig. 11.

In contrast to the strong effects on the dip-peak structure at larger driving, for weak driving (and the naive $F = k$ results) the effect of voltage fluctuations is nearly negligible. In particular, this can be observed (see Fig. 11) for higher resonances, where the frequency mismatch fluctuations $\propto \Delta V/k$ are reduced. Altogether, classical fluctuations, not unlike the quantum fluctuations due to the large α , lead to a broadening of the pronounced features predicted by

semiclassics, but the distortion of features can be quite strong. Despite the large impact of fluctuations, the highly nontrivial, complex driving dependence of the experimental and simulated Fano factors matches astonishingly well. Figure 3(b) of the main text demonstrates the high degree of theoretical understanding and experimental control Josephson-photonics systems offer in exploring this novel regime of strong-coupling quantum electrodynamics.

APPENDIX I: STRONG EMISSION REGIME OF A JOSEPHSON-PHOTONICS SYSTEM AT A MULTIPHOTON RESONANCE

The most striking feature of biasing a Josephson-photonics system at a multiphoton resonance is the emission of photon multiplets. This bunching is reflected in a photon Fano factor $F_k = k$, observed for the k -photon resonance at weak driving in accordance with the naive expectation. However, as Josephson energy and therefore emission get stronger and the resonator is not relaxing to its ground state between consecutive Cooper pair tunneling events, the dynamics becomes more complex and the behavior of the Fano factor of photonic emission [Fig. 3(c) of the main text] and the mean resonator occupation [Fig. 2(b) of the main text] become highly nontrivial. In essence, this is a consequence of two competing effects in the nonlinear terms of the Hamiltonian (i) At moderate E_J the k -parametric drive term, $\sim a^k + (a^\dagger)^k$ in Eq. (3), is strongly superlinear; in the fashion of stimulated emission, the tunneling matrix elements and the corresponding excitation rate are strongly enhanced, if there are already excitations present in the resonator. (ii) At stronger E_J , however, the Josephson nonlinearity formally encoded in the B_k operators in Eq. (3) suppresses the efficiency of the driving. In the classical limit, this is reflected in a Bessel function reaching its maximum [14], while for large α the same nonlinearity appears on a few-photon level and the resonator is effectively reduced to a few-level system (cf. Ref. [22] for the case $k = 1$).

Understanding the system in the semiclassical limit, $\alpha \rightarrow 0$ offers some insight into the complex dynamics, even for our case, where $\alpha \sim 1$. The generic dependence of the resonator occupation and of the Fano factor on E_J is visualized in Fig. 12. A detailed semiclassical analysis [14] shows that the scaled resonator occupation $\alpha \langle n \rangle$ undergoes a (bifurcation) transition to a saturation value for all k corresponding to the nonlinear suppression discussed as (ii) above. The corresponding threshold value E_J^{sat} above which $\alpha \langle n \rangle$ saturates has been discussed and derived in detail in Ref. [14]. For smaller E_J , the first and second resonance, $k = 1$ and $k = 2$, differ from $k \geq 3$.

For the $k = 1$ resonance, the occupation continuously increases with the E_J (quadratically, as expected in the weak E_J limit, where the Josephson coupling reduces to a linear drive). For the conventional parametric ($k = 2$) resonance, emission is suppressed for low E_J until a continuous onset above a parametric threshold value

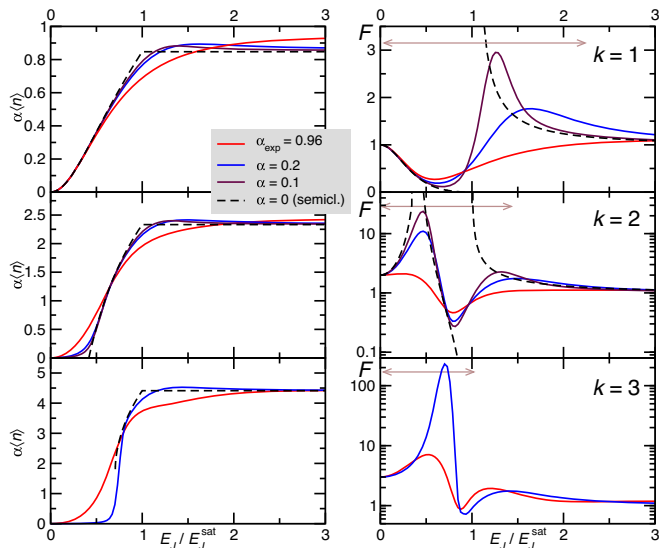


FIG. 12. Strong emission at multiphoton resonances, $k = 1, 2, 3$. Scaled occupation $\alpha\langle n \rangle$ (left) and Fano factor F of photon emission (right). Beyond the weak driving limit, the nonlinear dynamics is complex and shows two transitions (for $k \geq 2$): a saturation transition at $E_J/E_J^{\text{sat}} \equiv 1$ and a parametric transition at lower E_J (see Ref. [14] for derivations and details). While transitions are nonanalytic in the semiclassical limit, $\alpha \rightarrow 0$ (dashed), higher values of α progressively smoothen them and yield emission below the parametric threshold according to a rate picture of dynamical Coulomb blockade [cf. Eq. (3) and Fig. 2(b) of the main text]. The Fano factor starting from the naive bunch size, $F = k$, goes through a peak around the parametric threshold and a dip-peak structure around the saturation transition to settle at $F = 1$ for very strong driving. The ranges of drivings shown in Fig. 3(c) of the main text are marked by arrows.

[14], while for $k \geq 3$ at threshold the occupation jumps from zero to a finite value in the semiclassical limit. In Fig. 2(b) of the main text, which (because $\alpha \sim 1$) is far from the semiclassical limit, the parametric behavior manifests as a clear upward turn of the numerical results (solid lines) compared to the rate equation result of Eq. (3) in the main text (dashed lines), valid only in the low E_J limit.

For the Fano factor, one generically finds a peak around the parametric threshold, which has been described for $k = 2$ as bursts [40], each encompassing multiple pairs of photons. A semiclassical analysis is possible beyond the parametric threshold and finds a sudden switching of the noise. Noise and Fano factor vanish just below the saturation threshold, while they diverge above. This behavior has been explained in Ref. [37] as a generic result of a certain type of nonlinear driving Hamiltonian, where the nature of the fixed point and the corresponding fluctuation properties (amplitudes and correlation times) change abruptly.

The impact of quantum fluctuations for large α masks all sharp transitions predicted by semiclassics. Besides blurring all transitions, quantum fluctuations may also allow dynamical transitions between solutions and crucially affect certain observables [41].

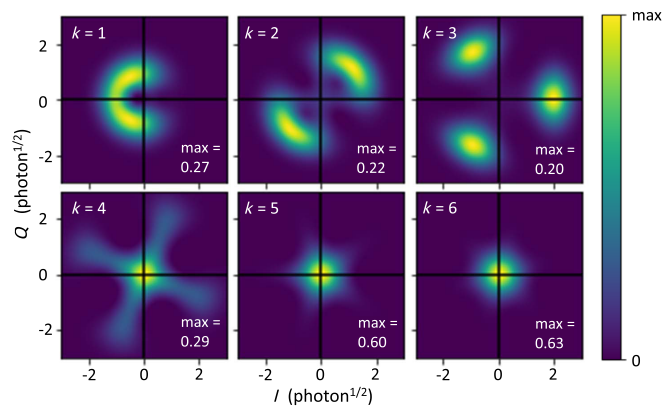


FIG. 13. Simulated intracavity field Wigner function with the parameters of run 2, at $E_J/h\nu_R = 0.142$. Amplitude of the Wigner function as a function of the two reduced quadratures of the field, for $k = 1-6$. Note that the color scale is bounded by the minimal value 0 indicating the absence of predicted Wigner negativity. The text in each panel indicates the maximal value of the color scale.

APPENDIX J: SIMULATED INTRACAVITY WIGNER FUNCTIONS

The k granularity of the microwave emission is not the only quantum feature of the emission process described in this work. Although we did not measure it, the field statistics is also non-Gaussian. The intracavity Wigner function has a k -fold symmetry, but apparently no Wigner negativity. Figure 13 displays, for instance, the Wigner functions obtained from the master equation simulations done for Fig. 2(b) at the highest Josephson energy $E_J/h\nu_R = 0.142$ (vertical dotted line in the figure). The k symmetry is clearly visible from $k = 2$ to 5, the very low occupation at $k = 6$ making the sixfold symmetry barely visible. At $k = 1$, the system is close to saturation and the Wigner function gets deformed compared to the displaced ground state simulated at low E_J (not shown), as for a linearly driven damped oscillator.

-
- [1] C. Cohen-Tannoudji, J. Dupont-Roc, and G. W. Grynberg, *Introduction to Quantum Electrodynamics* (Wiley-Interscience, New York, 1989).
 - [2] M. Corona, K. Garay-Palmett, and A. B. U'Ren, *Third-Order Spontaneous Parametric Down-Conversion in Thin Optical Fibers as a Photon-Triplet Source*, *Phys. Rev. A* **84**, 033823 (2011).
 - [3] C. W. Sandbo Chang, C. Sabín, P. Forn-Díaz, F. Quijandría, A. M. Vadiraj, I. Nsanzeza, G. Johansson, and C. M. Wilson, *Observation of Three-Photon Spontaneous Parametric Down-Conversion in a Superconducting Parametric Cavity*, *Phys. Rev. X* **10**, 011011 (2020).
 - [4] G.-L. Ingold and Y. V. Nazarov, *Charge Tunneling Rates in Ultrasmall Junctions*, in *Single Charge Tunneling*, edited by H. Grabert and M. H. Devoret (Plenum, New York, 1992).

- [5] G. B. Lesovik and R. Loosen, *On the Detection of Finite-Frequency Current Fluctuations*, *J. Exp. Theor. Phys. Lett.* **65**, 295 (1997).
- [6] Arne L. Grimsmo, Farzad Qassemi, Bertrand Reulet, and Alexandre Blais, *Quantum Optics Theory of Electronic Noise in Coherent Conductors*, *Phys. Rev. Lett.* **116**, 043602 (2016).
- [7] M. Hofheinz, F. Portier, Q. Baudouin, P. Joyez, D. Vion, P. Bertet, P. Roche, and D. Esteve, *Bright Side of the Coulomb Blockade*, *Phys. Rev. Lett.* **106**, 217005 (2011).
- [8] A. Cottet, T. Kontos, and B. Douçot, *Electron-Photon Coupling in Mesoscopic Quantum Electrodynamics*, *Phys. Rev. B* **91**, 205417 (2015).
- [9] Olesia Dmytruk, Mircea Trif, Christophe Mora, and Pascal Simon, *Out-of-Equilibrium Quantum Dot Coupled to a Microwave Cavity*, *Phys. Rev. B* **93**, 075425 (2016).
- [10] C. Mora, C. Altimiras, P. Joyez, and F. Portier, *Quantum Properties of the Radiation Emitted by a Conductor in the Coulomb Blockade Regime*, *Phys. Rev. B* **95**, 125311 (2017).
- [11] C. Altimiras, F. Portier, and P. Joyez, *Interacting Electrodynamics of Short Coherent Conductors in Quantum Circuits*, *Phys. Rev. X* **6**, 031002 (2016).
- [12] J. Leppäkangas, G. Johansson, M. Marthaler, and M. Fogelström, *Input-Output Description of Microwave Radiation in the Dynamical Coulomb Blockade*, *New J. Phys.* **16**, 015015 (2014).
- [13] Juha Leppäkangas, Göran Johansson, Michael Marthaler, and Mikael Fogelström, *Nonclassical Photon Pair Production in a Voltage-Biased Josephson Junction*, *Phys. Rev. Lett.* **110**, 267004 (2013).
- [14] A. D. Armour, M. P. Blencowe, E. Brahim, and A. J. Rimberg, *Universal Quantum Fluctuations of a Cavity Mode Driven by a Josephson Junction*, *Phys. Rev. Lett.* **111**, 247001 (2013).
- [15] Vera Gramich, Björn Kubala, Selina Rohrer, and Joachim Ankerhold, *From Coulomb-Blockade to Nonlinear Quantum Dynamics in a Superconducting Circuit with a Resonator*, *Phys. Rev. Lett.* **111**, 247002 (2013).
- [16] C. W. J. Beenakker and H. Schomerus, *Counting Statistics of Photons Produced by Electronic Shot Noise*, *Phys. Rev. Lett.* **86**, 700 (2001).
- [17] C. W. J. Beenakker and H. Schomerus, *Antibunched Photons Emitted by a Quantum Point Contact Out of Equilibrium*, *Phys. Rev. Lett.* **93**, 096801 (2004).
- [18] A. V. Lebedev, G. B. Lesovik, and G. Blatter, *Statistics of Radiation Emitted from a Quantum Point Contact*, *Phys. Rev. B* **81**, 155421 (2010).
- [19] I. C. Fulga, F. Hassler, and C. W. J. Beenakker, *Nonzero Temperature Effects on Antibunched Photons Emitted by a Quantum Point Contact Out of Equilibrium*, *Phys. Rev. B* **81**, 115331 (2010).
- [20] Fabian Hassler and Daniel Otten, *Second-Order Coherence of Microwave Photons Emitted by a Quantum Point Contact*, *Phys. Rev. B* **92**, 195417 (2015).
- [21] A. Grimm, F. Blanchet, R. Albert, J. Leppäkangas, S. Jebari, D. Hazra, F. Gustavo, J.-L. Thomassin, E. Dupont-Ferrier, F. Portier, and M. Hofheinz, *Bright On-Demand Source of Antibunched Microwave Photons Based on Inelastic Cooper Pair Tunneling*, *Phys. Rev. X* **9**, 021016 (2019).
- [22] C. Rolland, A. Peugeot, S. Dambach, M. Westig, B. Kubala, Y. Mukharsky, C. Altimiras, H. le Sueur, P. Joyez, D. Vion, P. Roche, D. Esteve, J. Ankerhold, and F. Portier, *Antibunched Photons Emitted by a dc-Biased Josephson Junction*, *Phys. Rev. Lett.* **122**, 186804 (2019).
- [23] M. C. Cassidy, A. Bruno, S. Rubbert, M. Irfan, J. Kammhuber, R. N. Schouten, A. R. Akhmerov, and L. P. Kouwenhoven, *Demonstration of an ac Josephson Junction Laser*, *Science* **355**, 939 (2017).
- [24] Frans Godschalk, Fabian Hassler, and Yuli V. Nazarov, *Proposal for an Optical Laser Producing Light at Half the Josephson Frequency*, *Phys. Rev. Lett.* **107**, 073901 (2011).
- [25] Frans Godschalk and Yuli V. Nazarov, *Lasing at Half the Josephson Frequency with Exponentially Long Coherence Times*, *Phys. Rev. B* **87**, 094511 (2013).
- [26] Frans Godschalk and Yuli V. Nazarov, *Light-Superconducting Interference Devices*, *Phys. Rev. B* **89**, 104502 (2014).
- [27] S. Jebari, F. Blanchet, A. Grimm, D. Hazra, R. Albert, P. Joyez, D. Vion, D. Estève, F. Portier, and M. Hofheinz, *Near-Quantum-Limited Amplification from Inelastic Cooper-Pair Tunnelling*, *National electronics review* **1**, 223 (2018).
- [28] Udon C. Mendes, Sébastien Jezouin, Philippe Joyez, Bertrand Reulet, Alexandre Blais, Fabien Portier, Christophe Mora, and Carles Altimiras, *Parametric Amplification and Squeezing with an ac- and dc-Voltage Biased Superconducting Junction*, *Phys. Rev. Applied* **11**, 034035 (2019).
- [29] Jean-Charles Forgues, Christian Lupien, and Bertrand Reulet, *Experimental Violation of Bell-like Inequalities by Electronic Shot Noise*, *Phys. Rev. Lett.* **114**, 130403 (2015).
- [30] Audrey Cottet, Zaki Leghtas, and Takis Kontos, *Theory of Interactions between Cavity Photons Induced by a Mesoscopic Circuit*, *Phys. Rev. B* **102**, 155105 (2020).
- [31] A. Peugeot, G. Ménard, S. Dambach, M. Westig, B. Kubala, Y. Mukharsky, C. Altimiras, P. Joyez, D. Vion, P. Roche, D. Esteve, P. Milman, J. Leppäkangas, G. Johansson, M. Hofheinz, J. Ankerhold, and F. Portier, *Generating Two Continuous Entangled Microwave Beams Using a dc-Biased Josephson Junction*, *Phys. Rev. X* **11**, 031008 (2021).
- [32] Jérôme Estève, Marco Aprili, and Julien Gabelli, *Quantum Dynamics of a Microwave Resonator Strongly Coupled to a Tunnel Junction*, [arXiv:1807.02364](https://arxiv.org/abs/1807.02364).
- [33] Gianluca Aiello, *Quantum Dynamics of a High Impedance Cavity Strongly Coupled to a Josephson Junction*, Ph.D. thesis, Paris-Saclay University, 2021.
- [34] Simon Dambach, Bjorn Kubala, Vera Gramich, and Joachim Ankerhold, *Time-Resolved Statistics of Nonclassical Light in Josephson Photonics*, *Phys. Rev. B* **92**, 054508 (2015).
- [35] Patrick P. Hofer, J.-R. Souquet, and A. A. Clerk, *Quantum Heat Engine Based on Photon-Assisted Cooper Pair Tunneling*, *Phys. Rev. B* **93**, 041418(R) (2016).
- [36] C. Emary, C. Pörtl, A. Carmele, J. Kabuss, A. Knorr, and T. Brandes, *Bunching and Antibunching in Electronic Transport*, *Phys. Rev. B* **85**, 165417 (2012).
- [37] Andrew D. Armour, Björn Kubala, and Joachim Ankerhold, *Noise Switching at a Dynamical Critical Point in a Cavity-Conductor Hybrid*, *Phys. Rev. B* **96**, 214509 (2017).

- [38] M. Hofheinz, H. Wang, M. Ansmann, R. C. Bialczak, E. Lucero, M. Neeley, A. D. O'Connell, D. Sank, J. Wenner, J. M. Martinis, and A. N. Cleland, *Synthesizing Arbitrary Quantum States in a Superconducting Resonator*, *Nature (London)* **459**, 546 (2009).
- [39] S. Krastanov, V. V. Albert, C. Shen, C.-L. Zou, R. W. Heeres, B. Vlastakis, R. J. Schoelkopf, and L. Jiang, *Universal Control of an Oscillator with Dispersive Coupling to a Qubit*, *Phys. Rev. A* **92**, 040303(R) (2015).
- [40] Ciprian Padurariu, Fabian Hassler, and Yuli V. Nazarov, *Statistics of Radiation at Josephson Parametric Resonance*, *Phys. Rev. B* **86**, 054514 (2012).
- [41] B. Lang and A. D. Armour, *Multi-photon resonances in Josephson junction-cavity circuits*, *New J. Phys.* **23**, 033021 (2021).